Strain induced polymorphism and band structure modulation in low-temperature 2,7-dioctyl[1]benzothieno[3,2-b][1]benzothiophene single crystal

Jianfeng Chen[1], Wen Shi[1], Yuqian Jiang[2], Dong Wang[1]* & Zhigang Shuai[1,3,4]*

[1]*MOE Key Laboratory of Organic OptoElectronics and Molecular Engineering, Department of Chemistry, Tsinghua University, Beijing 100084, China*
[2]*National Center for Nanoscience and Technology, Beijing 100190, China*
[3]*Key Laboratory of Organic Solids, Beijing National Laboratory for Molecular Science (BNLMS), Institute of Chemistry, Chinese Academy of Sciences, Beijing 100190, China*
[4]*Collaborative Innovation Center of Chemistry for Energy Materials, Xiamen University, Xiamen 351005, China*

Organic semiconductors are inherently soft, making it possible to increase their mobilities by strains. Such a unique feature can be exploited directly in flexible electronics for improved device performance. The 2,7-dioctyl[1]benzothieno[3,2-b][1]-benzothiophene derivative, C8-BTBT is one of the best small-molecule hole transport materials. Here, we demonstrated its band structure modulation under strains by combining the non-equilibrium molecular dynamics simulations and first-principles calculations. We found that the C8-BTBT lattice undergoes a transition from monoclinic to triclinic crystal system at the temperature below 160 K. Both shear and uniaxial strains were applied to the low-temperature triclinic phase of C8-BTBT, and polymorphism was identified in the shear process. The band width enhancement is up to 8% under 2% of compressive strain along the x direction, and 14% under 4% of tensile strain along the *y* direction. The band structure modulation of C8-BTBT can be well related to its herringbone packing motifs, where the edge to face and edge to edge pairs constitute two-dimensional charge transport pathways and their electronic overlaps determine the band widths along the two directions respectively. These findings pave the way for utilizing strains towards improved performance of organic semiconductors on flexible substrates, for example, by bending the substrates.

charge transport, shear strain, polymorphism, band structure modulation, flexible electronics

1   Introduction

High performance organic electronic devices have been sought by academic and industrial communities for decades due to their bright outlooks in flat-panel displays [1,2], radio-frequency identification tags [3,4], complementary integrated circuits [5–7], biological and medical applications [8–13] and other advantages such as ease of fabrication, low-cost, large-area production, and mechanical flexibility [14–19]. However, charge carrier mobility is still the key barrier that hinders organic electronic devices to broader applications [20]. Factors limiting the mobility of organic semiconductors include their chemical component, molecular packing structure and crystallinity. The mobility of a material with specific constituents can be very sensitive to its

---

*Corresponding authors (email: dong913@tsinghua.edu.cn; zgshuai@tsinghua.edu.cn)

molecular packing structure. Due to the weak van der Waals interactions between organic molecules, polymorphism often shows up during the fabrication process. Many methods and techniques including air-flow [21,22], roll transfer printinf [23], solvent additives [24], solvent and polymer matrix [25], solution shearing [26,27], and fluid-enhanced crystal engineering [28] have been developed to increase the alignment of crystallites and tune the molecular packing structure towards a better charge transport performance. Bao's group [27–31] fabricated series of organic thin film transistors by various solution processes. Among these, solution shearing has been manifested as one of the most effective methods to tune the molecular packing in organic thin films. For example, the π-π stacking distance of TIPS-pentacene (6,13-bis(triisopropylsilylethynyl) pentacene) was decreased from 3.33 Å to 3.08 Å at a shear speed of 8 mm s^{-1}, and the mobility of sheared thin film was increased to 1.5 cm^2 V^{-1} s^{-1} due to the increased electronic overlap between neighboring molecules. The mobility of TIPS-pentacene was even increased to 11 cm^2 V^{-1} s^{-1} by combining fluid-enhanced crystal engineering and solution shearing methods [28].

Thienoacenes, such as [1]benzothieno[3,2-b][1]benzothiophenes (BTBTs), have appropriate HOMO spatial distribution for effective intermolecular orbital overlap, and exhibit excellent hole transport properties [32]. Bao's group [30] has reported growth of highly aligned 2,7-dioctyl[1]-benzothieno[3,2-b][1]benzothiophene (C$_8$-BTBT) thin film by a novel off-center spin-coating method, which showed a significantly increased transistor hole mobility up to 43 cm^2 V^{-1} s^{-1}. They found that structures grown by solution shearing and off-center spin-coating methods are meta-stable, and would restore to the equilibrium after solvent vapor annealing and thermal annealing. The alternative approach to tune the molecular packing is by applying strains directly to organic semiconductors from bending the flexible substrates of devices. In a previous work [33], we studied the relationship between shear strain, molecular packing, and charge carrier mobility in TIPS-pentacene, and predicted one order-of-magnitude increase of the mobility through a combination of shear and tensile strains. TIPS-pentacene adopts a brick-wall packing structure, whereas C$_8$-BTBT adopts a herringbone packing structure, and its response to strain has never been looked over before. In this work, we showed the strain-induced band structure modulation in C$_8$-BTBT by combining non-equilibrium molecular dynamics (MD) simulations and density functional theory (DFT) calculations. We identified a new phase in the shear process with almost identical energy and band width. We discussed the band width enhancement under shear and uniaxial strains with the packing motif of C$_8$-BTBT and transfer integrals.

2 Method

2.1 Model setup

The crystal structure of C$_8$-BTBT at 293.2 K was taken from the experiment [34]. The lattice is monoclinic with parameters being $a=5.927$Å, $b=7.880$Å, $c=29.180$Å, $\alpha=90°$, $\beta=92.443°$, $\gamma=90°$. In the C$_8$-BTBT crystal, conjugated rings with delocalized electrons are distributed in the *ab* plane, and long alkyl chains are oriented along the *c* direction, so the *ab* plane has constituted the two-dimensional (2D) charge transport channel of C$_8$-BTBT. This has been manifested in the band structure of C$_8$-BTBT, which exhibits anisotropic and 2D character [35]. The unit cell was such oriented in the Cartesian coordinate system that the crystal axis *a* is along *x*, and the crystal axis *b* is along *y*, as shown in Figure 1. A super cell of 7×7×3 was set up to eliminate the boundary effect in the molecular dynamics simulations with the general amber force filed (GAFF) [36]. GAFF is appropriate for describing molecular interactions in small-molecule organic crystals, as demonstrated in our previous studies [33,35,37]. The geometry optimization and electrostatic potential calculation were performed by the HF/6-31G(d) method within the Gaussian software package [38]. The partial charge on each atom was derived by the restrained electrostatic potential (RESP) fitting method [39,40].

2.2 MD simulation

All the MD simulations were performed with the LAMMPS software package [41]. Energy minimization and NPT relax-
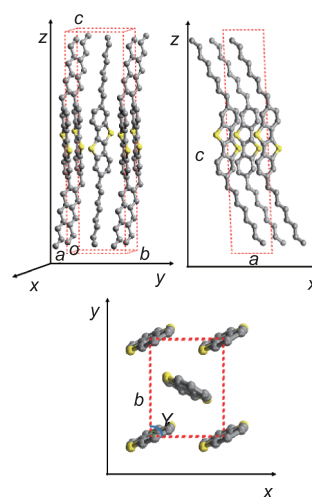

Figure 1 The herringbone packing of C$_8$-BTBT and its orientation in the Cartesian coordinate system. The experimental lattice parameters are $a=5.927$Å, $b=7.880$Å, $c=29.180$Å, $\alpha=90°$, $\beta=92.443°$, $\gamma=90°$. The crystal axis *a* is along the *x* direction and *b* is along the *y* direction, which constitute the 2D charge transport channel. The crystal axis *c*, which is the alkyl chain elongation direction, is in the *xz* plane.

ation were carried out for the super cell to release the inner stress before inducing strains to the crystal. The pressure and temperature were maintained in the NPT simulation by the Nosé-Hoover thermostat and barostat [42,43]. Periodic boundary conditions were applied to the finite simulation box to eliminate the boundary effect. The average lattice parameters of C8-BTBT relaxed at the temperature from 300 K to 1 K at an interval of 20 K and the pressure of 0 atm were provided in Table S1 of the Supporting Information online (SI). At 300 K, the relaxed lattice parameters are a=6.07 Å, b=7.87 Å, c=28.92 Å, α=89.98°, β=91.98°, γ=89.99°. The lattice remains monoclinic, and the deviation from room-temperature crystal structure is within 2%, indicating the validity of the force field. The GAFF has been applied previously by us to calculate the lattice thermal conductivity of C8-BTBT, and the result was reasonable [35]. During the thermal cooling, C8-BTBT crystal undergoes a phase transition from monoclinic to triclinic at 160 K. After the relaxation at 1 K and 0 atm, the average lattice parameters are a=6.57Å, b=7.01 Å, c=27.34 Å, α=84.92°, β=94.48°, γ=93.42°. Although the crystal lattice has transformed from monoclinic to triclinic, C8-BTBT molecules still pack in the herringbone structure. The X-ray diffraction pattern of room-temperature monoclinic and low-temperature triclinic crystal structures was shown in Figure S1 of the SI. Since the band structure modulation by strains and structure-property relationship are interested, the strain was applied to the low-temperature C8-BTBT single crystal to avoid dynamic disorder.

After the NPT relaxation, shear and uniaxial strains were induced respectively to the crystal during the non-equilibrium MD simulations at 1 K. In this process, either shear strain in the xy direction or uniaxial strain along the x or y direction was applied by deforming the simulation box at a rate of 10^7 s^{-1}, and at the same time releasing the stress induced in all other directions. In the shear process, the shear strain ε_{xy} was induced by tuning the projection of b along the x axis, which is equivalent to changing the angle γ according to the engineer definition. ε_{xy}>0 represents increasing the projection of b along the positive x direction, ε_{xy}<0 represents decreasing the projection of b along the positive x direction, as illustrated in Figure 2(a). The crystal was sheared from ε_{xy}=−0.1to ε_{xy}=0.22 and during the shear simulation, the xy component of stress tensor p_{xy} was recorded as a response to the shear strain. The uniaxial strain was induced by tuning the projection of a (or b) along the x (or y) direction, which was defined as the ratio of the projection change to the original projection along a specific direction, x or y. ε_{xx}>0 (ε_{yy}>0) represents tensing along the x (or y) direction, and ε_{xx}<0 (ε_{yy}<0) represents compressing along the x (or y) direction, as shown in Figure 2(b) and (c). Similarly, the xx or yy component of the stress tensor p_{xx} or p_{yy} was recorded respectively as a response to ε_{xx} from −0.02 to 0.16, or ε_{yy} from −0.12 to 0.04.
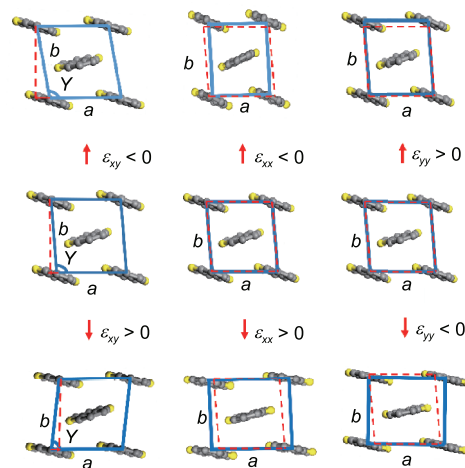

Figure 2   Illustration of lattice deformations induced by strains. *Left panel:* shear strain in the xy direction. The inter-axial angle γ decreases with the shear strain ε_{xy}>0, while it increases with the shear strain ε_{xy}<0. *Middle panel:* uniaxial strain in the x direction. When the crystal is tensed along the x direction, uniaxial strain ε_{xx}>0, and the distance between the conjugated rings increases along the lattice axis a, when the crystal is compressed, uniaxial strain ε_{yy}<0. *Right panel:* uniaxial strain in the y direction. Similar rules apply.

2.3   Band structure and transfer integral calculation.

The deformed crystal structures were extracted at a strain interval of 0.02 from the non-equilibrium MD simulations. The central unit cell parameters of each super cell under a specific strain were used for the subsequent band structure calculation to explore the impact of strain on the charge transport property. The atomic position was optimized before the band structure calculation. Both optimization and band structure calculation were performed by the projector augmented wave (PAW) method with the Perdew-Burke-Ernzerhof including dispersion (PBE-D) exchange correlation functional implemented in the Vienna *ab initio* simulation package (VASP 5.3.2) [44–46]. The cutoff energy for the plane-wave basis was 600 eV. The convergence criterion of the total energy in the self-consistent field iteration was set to be 10^{-5} eV, the Monkhorst-Pack k-mesh for ionic relaxations was 4×4×1 and for the single-point energy and charge density calculations was 8×8×2. The cutoff radius for pair interactions was set to be 50 Å. The tetrahedron method with Blöch corrections was used for smearing.

To understand the relationship between the molecular packing and the charge transport property of C₈-BTBT, intermolecular transfer integral of sheared structures has been calculated by the site-energy-corrected coupling method, which can be expressed as

$$V_{mn} = [V_{mn}^0 - (1/2)(e_m + e_n)O_{mn}]/[1 - O_{mn}^2] \tag{1}$$

where $e_m = \phi_m|H|\phi_m$, $V_{mn}^0 = \phi_m|H|\phi_n$, and O_{mn}= $\phi_m|O|\phi_n$. $\phi_{m(n)}$ is the frontier molecular orbital of an

isolated molecule $m(n)$ in the dimer. H represents the dimer Hamiltonian and O is the overlap matrix. Intermolecular transfer integrals for the nearest neighbor pairs were calculated by the PW91PW91/6-31G(d) method [47], based on previous benchmark studies [48].

3 Results and discussion

3.1 Mechanical response

In the shear process, the angle γ between a and b crystal axis varied from 99.12° to 80.77°. In the tensile process, the cell length increased in one direction while decreased in the other. The length of a increased from 6.44 Å to 7.62 Å when tensed along the x direction, while b decreased from 7.12 Å to 6.75 Å. Similarly, when tensed along the y direction b increased from 6.18 Å to 7.30 Å while a decreased from 7.23 Å to 6.35 Å.

The stress-strain relationship obtained in the non-equilibrium MD simulation was shown in Figure 3. Those structures in the elastic region of the stress-strain curve were extracted for band structure calculations. In the shear process, there appear two elastic regions in the stress-strain curve, one is from $\varepsilon_{xy}=-0.1$ to $\varepsilon_{xy}=0.02$, and the other is from $\varepsilon_{xy}=-0.1$ to $\varepsilon_{xy}=0.22$. The shear elastic constant γ_{xy}, defined as the slope of the stress-strain curve, is 2.09 GPa and 2.45 GPa respectively. Due to the weak van der Waals interactions between molecules, the elastic constant of organic crystals is smaller than inorganic crystals. The elastic region in the uniaxial stress-strain curves is defined by ε_{xx} from –0.02 to 0.16, and ε_{yy} from –0.12 to 0.04 respectively. The uniaxial elastic constants $\gamma_{xx}=4.58$ GPa and $\gamma_{yy}=5.59$ GPa are twice as large as the shear elastic constant. As compared to TIPS-pentacene which adopts a brick-wall packing, C_8-BTBT crystal is less stiff, especially in the shear direction since the shear elastic constant of C_8-BTBT is half that of TIPS-pentacene.

3.2 C_8-BTBT polymorphism

The linear region in the shear stress-strain curve, from $\varepsilon_{xy}=0.1$ to $\varepsilon_{xy}=0.22$, is identified as a new phase with slightly different shear elastic constant. The structures located in the linear region with ε_{xy} from –0.1 to 0.02 are denoted phase 1 and those in the linear region with ε_{xy} from 0.1 to 0.22 are denoted phase 2. The stress is zero at $\varepsilon_{xy}=0$ and $\varepsilon_{xy}=0.12$, which represent respectively equilibrium structures of the two phases. The sheared structures in phase 1 and phase 2 were relaxed at the temperature of 1 K and the pressure of 0 atm in the NPT ensemble. The lattice parameters of relaxed structures restore either to $a=6.56$ Å, $b=7.02$ Å, $c=27.53$Å, $\alpha=84.84°$, $\beta=94.47°$, $\gamma=93.48°$, which is the original cell parameters at $\varepsilon_{xy}=0$, or to $a=6.56$ Å, $b=7.02$ Å, $c=27.53$ Å, $\alpha=95.1°$, $\beta=94.47°$, $\gamma=86.52°$, which is the cell parameters at
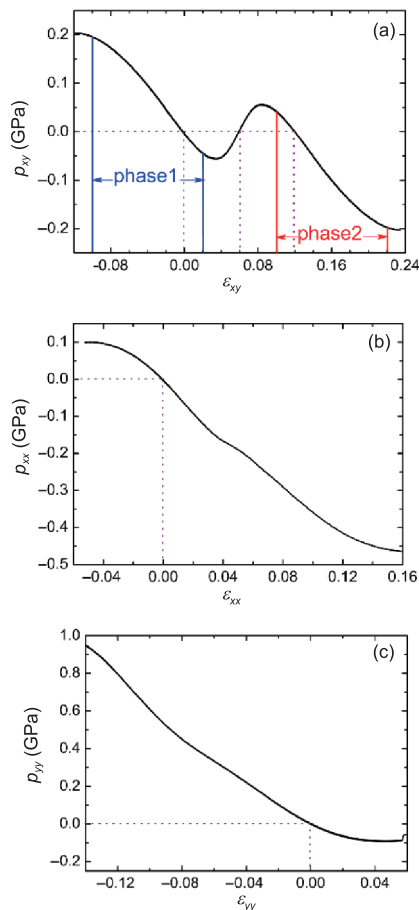
Figure 3 Stress-strain curves from non-equilibrium MD simulations. (a) Shear stress-strain curve shows two elastic regions, denoted as phase 1 and phase 2 respectively. The shear strain changes from $\varepsilon_{xy}=-0.1$ to $\varepsilon_{xy}=0.22$. (b) Uniaxial stress in the x direction with strain from $\varepsilon_{xx}=-0.02$ to $\varepsilon_{xx}=0.16$. (c) Uniaxial stress in the y direction with strain from $\varepsilon_{yy}=-00.12$ to $\varepsilon_{xy}=0.04$.

$\varepsilon_{xy}=0.12$. The sheared structures in phase 1 were relaxed to the former, whereas those in phase 2 were relaxed to the latter. The atomic positions in the two crystal structures at $\varepsilon_{xy}=0$ and $\varepsilon_{xy}=0.12$ were optimized first-principly within VASP and their energies turned out almost identical. Undoubtedly, a new phase showed up in the shear simulation. The only difference between the two sets of lattice parameters is the change of α and γ angles to their complementary angles, so the two phases identified are related to the triclinic lattice of C_8-BTBT under the low temperature. Coincidentally, a new phase of C_8-BTBT was identified earlier by thermal annealing in Bao's experiment [49]. Their new phase was distinguished by changes of the in-plane peak positions (Q_{xy}) and peak widths of the two major diffractions in 2D grazing incidence X-ray diffraction (GIXD) experiments. Unfortunately, it's hard to fully resolve the lattice structural change by such few peak information, so we cannot ascertain whether the polymorphism induced by strain here under the low temperature is similar to that induced by thermal annealing.

3.3   Band structure modulation

The band structure of unstrained C_8-BTBT was shown in Figure 4(a). The reciprocal coordinates of high-symmetry points are $\Gamma=(0, 0, 0)$, $Y=(0, 0.5, 0)$, $X=(0.5, 0, 0)$, and $Z=(0, 0, 0.5)$ respectively. Although the lattice of C_8-BTBT is triclinic, its deviation from the orthorhombic lattice is not large in the whole straining process, so ΓX, ΓY and ΓZ directions in the reciprocal space largely coincide with *a*, *b* and *c* directions in the real space. Electronic band structures of C_8-BTBT were modulated by shear and uniaxial strains. The band width and effective mass of strained structures extracted from non-equilibrium MD simulations were obtained by the DFT calculations. Since C_8-BTBT is a p-type organic semiconductor, we focus on the valence band only. In the shear process, the valence band width exhibits a parabolic dependence on the shear strain as shown in Figure 5(a). In phase 1, the band width along the ΓX direction increased from 184 meV to 436 meV and that along the ΓY direction increased from 161 meV to 352 meV with shear strain increasing from $\varepsilon_{xy}=-0.1$ to $\varepsilon_{xy}=0.02$, which shows that the band width has been increased effectively by shear strain. The band width of unstrained C_8-BTBT is 412 meV along the ΓX direction and 331 meV along the ΓY direction. Comparing with unstrained structure, the band width of sheared structure at $\varepsilon_{xy}=0.02$ has been enhanced by 24 meV along the ΓX direction and 21 meV along the ΓY direction, about 6% enhancement in both directions. In phase 2, the band width along the ΓX direction decreased from 436 meV to 189 meV

Figure 5   Valence band width modulation by strains. (a) Shear strain from $\varepsilon_{xy}=-0.1$ to $\varepsilon_{xy}=0.22$. (b) Uniaxial strain in the x direction from $\varepsilon_{xx}=-0.02$ to $\varepsilon_{xx}=0.16$. (c) Uniaxial strain in the y direction from $\varepsilon_{yy}=-0.12$ to $\varepsilon_{yy}=0.04$.

and that along the ΓY direction decreased from 349 meV to 156 meV with shear strain increasing from $\varepsilon_{xy}=0.1$ to $\varepsilon_{xy}=0.22$. The structure at shear strain $\varepsilon_{xy}=0.1$ shows the largest band width, which increases by 24 meV along the ΓX direction and 18 meV along the ΓY direction compared to unstrained structure of phase 2 at $\varepsilon_{xy}=0.12$.

As seen from the stress-strain curve in Figure 3(a), there locates between phase 1 and phase 2 a transient region from $\varepsilon_{xy}=0.04$ to $\varepsilon_{xy}=0.08$. The stress is zero at $\varepsilon_{xy}=0.06$, but this structure is unstable from its mechanical response to strain. The atomic position was optimized by VASP and the total energy was indeed 59 meV higher than that of phase 1 and phase 2. Though thermodynamically unstable, the structure at $\varepsilon_{xy}=0.06$ exhibits the largest band width of 458 meV along the ΓX direction and 379 meV along the ΓY direction. Compared to unstrained structure in either phase, the band width has increased by 46 meV along the ΓX direction and 49 meV along the ΓY direction with up to 15% enhancement.

In contrast, the valence band width of C_8-BTBT varies monotonically with uniaxial strain. When the crystal is
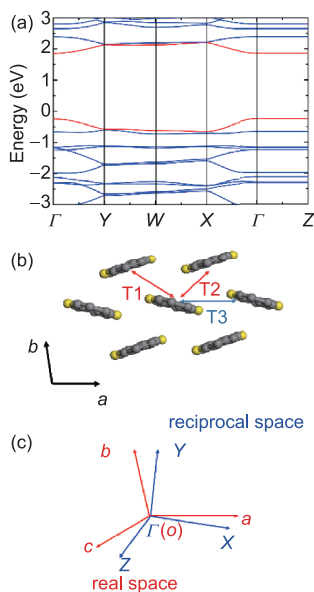
Figure 4   (a) Band structure of unstrained C_8-BTBT. The reciprocal coordinates of high-symmetry points are $\Gamma=(0,0,0)$, $Y=(0,0.5,0)$, $W=(0.5,0.5,0)$, $X=(0.5,0,0)$, $Z=(0,0,0.5)$ respectively. (b) Three main charge transport pathways including the edge to face T1 and T2, the edge to edge T3. (c) Relative orientation of reciprocal space and real space lattice vectors.
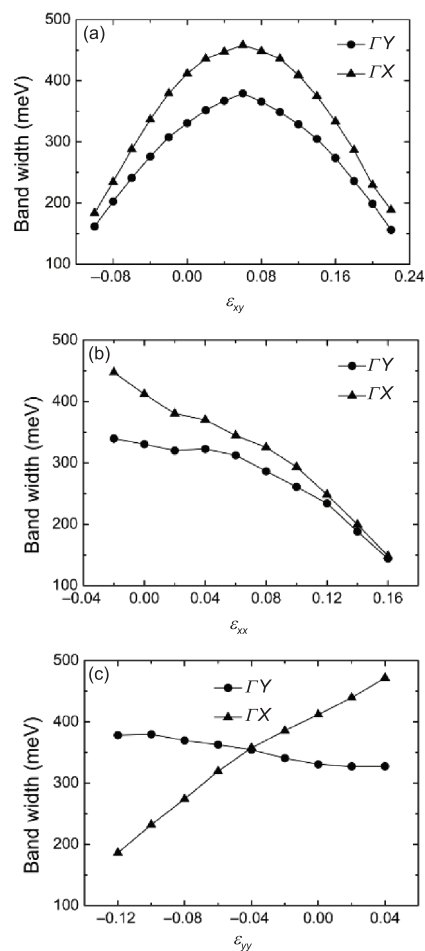
tensed along the x direction, the band width along the ΓX direction decreases from 447 meV to 149 meV, and that along the ΓY direction decreases from 340 meV to 144 meV with the tensile strain increasing from $\varepsilon_{xx}=-0.02$ to $\varepsilon_{xx}=0.16$. Comparing with the unstrained structure, the largest band width enhancement is 35 meV along the ΓX direction and 9 meV along the ΓY direction with $\varepsilon_{xx}=-0.02$, which is about 8% and 3% increase respectively. The band width variation showed the opposite trend when the crystal is tensed along the y direction. This can be understood largely from the Poisson effect, which states that when the crystal is tensed in the y direction, it tends to shrink in the other two directions. As a result, the band width along the ΓX direction increased from 186 meV to 472 meV, however, it decreased slightly along the ΓY direction from 378 meV to 327 meV with the tensile strain increasing from $\varepsilon_{yy}=-0.12$ to $\varepsilon_{yy}=0.04$. So the band anisotropy increased, which is different from the tensile process along the x direction. The largest band width increase along the ΓX direction is 60 meV with $\varepsilon_{yy}=0.04$ as compared to the unstrained structure, which is about 14% increase.

The valence band effective mass of strained structures was also obtained (Figure 6). In general, the larger the band width, the smaller the effective mass, which was verified by our data. In the shear process, the effective mass along the ΓY direction decreased from 6.13 m_e to 2.81 m_e, and that along the ΓX direction decreased from 4.19 m_e to 1.75 m_e with the shear strain increasing from $\varepsilon_{xy}=-0.1$ to $\varepsilon_{xy}=0.06$, whereas the effective mass along the ΓY direction increased from 2.81 m_e to 6.42 m_e, and that along the ΓX direction increased from 1.75 m_e to 4.03 m_e with the shear strain increasing from $\varepsilon_{xy}=0.06$ to $\varepsilon_{xy}=0.22$. The effective mass is the smallest at $\varepsilon_{xy}=0.06$ the unstable structure, and it is 8% reduction along the ΓY direction and 9% reduction along the ΓX direction as compared to the stable unstrained structure. In the tensile process, the effective mass exhibits a monotonic variation with strain. When the crystal was tensed along the x direction from $\varepsilon_{xx}=-0.02$ to $\varepsilon_{xx}=0.16$, the effective mass increased from 2.95 m_e to 8.93 m_e along the ΓY direction and from 1.85 m_e to 4.83 m_e along the ΓX direction. When the crystal was tensed along the y direction from $\varepsilon_{yy}=-0.12$ to $\varepsilon_{yy}=0.04$, the effective mass remained almost unchanged along the ΓY direction, and decreased from 7.32 m_e to 1.85 m_e along the ΓX direction.

Overall, by applying three forms of strains, the band width of C$_8$-BTBT has been effectively modulated. Under 6% of shear strain, the band width has increased by up to 46 meV and 49 meV in the ΓX and ΓY directions respectively. Under 2% of uniaxial compressive strain in the x direction, the band width has increased by 35 meV and 9 meV in the ΓX and ΓY directions respectively, while under 4% of uniaxial tensile strain in the y direction, it increases by as large as 60 meV in the ΓX direction. The magnitude of band width increase is comparable to that of transfer integral increase induced by
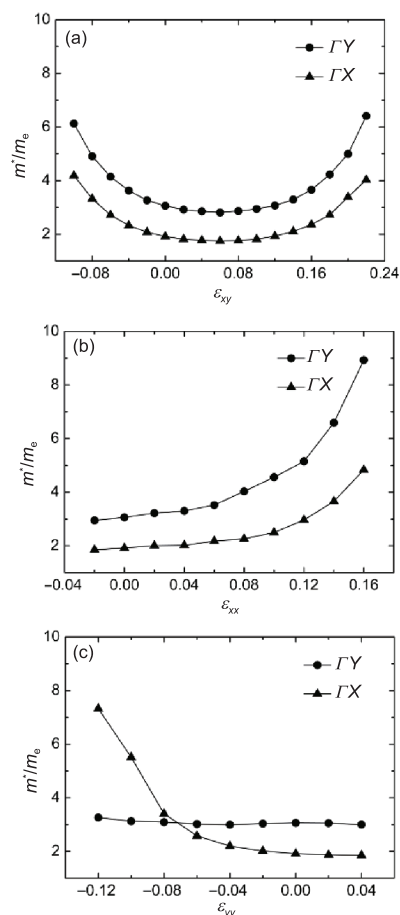

Figure 6 Valence band effective mass modulation under strains. (a) Shear strain from $\varepsilon_{xy}=-0.1$ to $\varepsilon_{xy}=0.22$. (b) Uniaxial strain in the x direction from $\varepsilon_{xx}=-0.12$ to $\varepsilon_{xx}=0.16$. (c) Uniaxial strain in the y direction from $\varepsilon_{yy}=-0.12$ to $\varepsilon_{yy}=0.04$.

shear and uniaxial strains in TIPS-pentacene, which ranges from 35 to 50 meV with shear or uniaxial strain up to 10% [33]. For TIPS-pentacene, the mobility increase induced by shear strain is as large as one order of magnitude, from 0.31 to 12 cm^2 V^{-1} s^{-1} by a combination of shear and uniaxial strains [34]. In contrast to C$_8$-BTBT, charge carriers in TIPS-pentacene are believed to adopt a hopping transport mechanism because the reorganization energy of TIPS-pentacene, ~220 meV, is much larger than the transfer integral, which is only a few meV in unstrained crystals. The band width of unstrained C$_8$-BTBT is 412 meV along the ΓX direction, and 331 meV along the ΓY direction. In TIPS-pentacene, the strain-induced transfer integral increase is more than 10 times, while the strain-induced band width increase is only 10% in C$_8$-BTBT. The unstrained C$_8$-BTBT has the effective mass of 1.92 m_e along the ΓX direction and 3.06 m_e along the ΓY direction. Under 6% of shear strain the effective mass is the smallest, which is 1.75 m_e and 2.81 m_e along the ΓX and ΓY directions respectively. The larger band width and smaller effective mass usually indicate the higher mobility. If assuming that

charge carrier scattering is the same, the mobility increase is expected to be 8% according to $\mu = e\tau / m^*$, where τ is the relaxation time.

3.4   Packing structure and transfer integral

Different from TIPS-pentacene that adopts a brick-wall packing and exhibits one-dimensional charge transport, C_8-BTBT adopts a herringbone packing structure and exhibits two-dimensional in-plane charge transport behavior. The transport pathways in C_8-BTBT have been illustrated in Figure 4(b). There are six nearest neighbors around the central C_8-BTBT, with three symmetry inequivalent transport channels denoted as edge to face T1, edge to face T2 and edge to edge T3 respectively. Of these, transfer integral of two edge to face pairs T1 and T2 is responsible for charge transport in the y direction, and that between edge to edge pair T3 is responsible for charge transport along the x direction. The molecular packing structure has been changed significantly under strain. In the shear process, the center-of-mass distance of T3 exhibit largely a parabolic variation with shear strain, in accord with the variation of band width along the ΓX direction, see Figure 7(a). In our previous study of TIPS-pentacene which adopts the edge to edge stacking, we showed that the transfer integral is determined not only by the inter-plane distance but also by the displacement along the long and short axis of conjugated core. In case of edge to edge packing T3 in C_8-BTBT, it seems that the electronic overlap between two conjugated rings is mainly determined by the center-of-mass distance between them, since there is little displacement along the long and short axis of BTBT core during the shear process. The center-of-mass distances of both T1 and T2 vary monotonically with shear strain, with that of T1 decreasing from 5.246 Å to 4.464 Å and that of T2 instead increasing from 4.463 Å to 5.247 Å when the shear strain increases from $\varepsilon_{xy}=-0.1$ to $\varepsilon_{xy}=0.22$. However as shown in Figure 8, transfer integrals of both T1 and T2 vary parabolically with shear strain, in line with the band width variation along the ΓY direction presented above in Figure 5(a). This indicates that for the edge to face packing as T1 and T2 the electronic overlap of the pair is not only determined by its centroid distance, but also by the orientation of conjugated rings. The band width in the ΓY direction is apparently governed by transfer integrals of both T1 and T2.

In the tensile process along the x direction, distance of T1 changes little and distance of T2 increases significantly from 4.668 Å to 5.112 Å with the tensile strain from $\varepsilon_{xx}=-0.02$ to $\varepsilon_{xx}=0.16$. As a result, the band width along the ΓY direction decreases. At the same time, distance of T3 increases from 6.44 Å to 7.623 Å so the band width along the ΓX direction also decreases. When the crystal is tensed along the y direction, again distance of T1 changes little and that of T2 increases slightly from 4.511 Å to 4.729 Å, so the band width
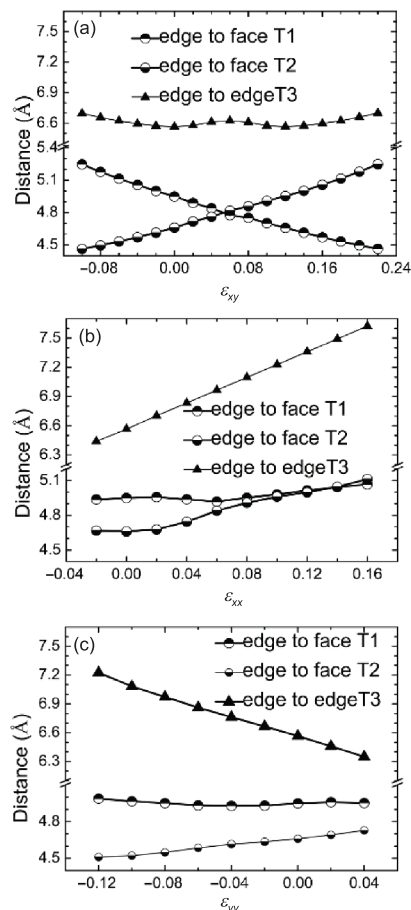

Figure 7   Center-of-mass distances between the nearest conjugated rings along three charge transport pathways modulated by shear and uniaxial strains. (a) Shear strain from $\varepsilon_{xy}=-0.1$ to $\varepsilon_{xy}=0.22$. (b) Uniaxial strain in the x direction from $\varepsilon_{xx}=-0.02$ to $\varepsilon_{xx}=0.16$. (c) Uniaxial strain in the y direction from $\varepsilon_{yy}=-0.12$ to $\varepsilon_{yy}=0.04$.

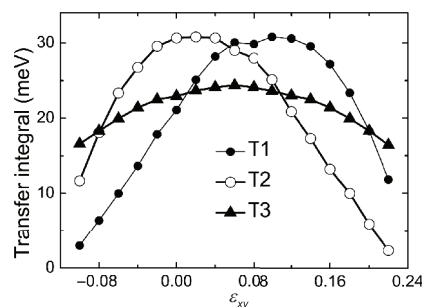**Figure 8**   Transfer integral changing with shear strain from $\varepsilon_{xy}=-0.1$ to $\varepsilon_{xy}=0.22$.

along the ΓY direction decreases. Simultaneously, distance of T3 decreases from 7.225 Å to 6.349 Å so the band width along the ΓX direction increases.

4   Conclusions

To conclude, we have shown that C_8-BTBT lattice under-

goes a transition from monoclinic to triclinic at the temperature below 160 K. Based on the low-temperature triclinic structure, we identified a new phase of C_8-BTBT during the non-equilibrium molecular dynamics simulations by applying the shear strain. This new phase is thermodynamically stable, and its band width is comparable to the original one. A thermodynamically unstable structure under 6% of shear strain with zero stress, locating between these two phases, exhibits the largest band width, with up to 15% enhancement as compared to the unstrained structure. The polymorphism of organic semiconductors is common since organic molecules are bound together by weak van der Waals interactions. Actually, a new phase of C_8-BTBT has been identified in Bao's experiment by thermal annealing.

We have observed significant band structure modulation under uniaxial strains during the non-equilibrium molecular dynamics simulations. The band width of C_8-BTBT shows as large as 8% enhancement under 2% of compressive strain in the x direction, and 14% enhancement under 4% of tensile strain in the y direction. In case of tensing along the y direction, the band anisotropy also increases significantly. The band width modulation was closely related to the packing motifs of C_8-BTBT, where the two edge to face pairs T1 and T2 constitute main charge transport pathways in the y direction, while the edge to edge pair T3 is responsible for charge transport along the x direction. The variation of transfer integrals between the edge to face pairs T1 and T2 with strains is in line with the variation of band width along the ΓY direction, and that between the edge to edge pair T3 is in line with the band width variation along the ΓX direction.

In a previous work, we studied the pressure-dependent mobility of naphthalene single crystal from 1 atm to 2.1 GPa at room temperature, and found that the pressure increases the phonon frequency and lowers the electron-phonon coupling, leading to a linear increase of hole mobility with increasing pressure [50]. The lattice parameters of naphthalene single crystal under various pressures were determined experimentally. The pressure is isotropic while the strain applied in the current study is uniaxial, and can be easily induced in the fabrication process. Our findings here have laid the foundation for utilizing strains to improve the performance of organic semiconductors built on flexible substrates. For example, a recent experiment showed that under homogeneous strain of 3%, induced by bending the flexible substrates, the field-effect mobility of C_{10}-DNBDT-NW single crystal increased by 70%, from 9.7 to 16.5 cm² V⁻¹ s⁻¹ [51].

Conflict of interest   Conflict of interest The authors declare that they have no conflict of interest.

Supporting information   The supporting information is available online at http://chem.scichina.com and http://link.springer.com/journal/11426. The supporting materials are published as submitted, without typesetting or editing. The responsibility for scientific accuracy and content remains entirely with the authors.

1   Rogers JA, Bao Z. *J Polym Sci A Polym Chem*, 2002, 40: 3327–3334
2   Gelinck GH, Huitema HEA, van Veenendaal E, Cantatore E, Schrijnemakers L, van der Putten JBPH, Geuns TCT, Beenhakkers M, Giesbers JB, Huisman BH, Meijer EJ, Benito EM, Touwslager FJ, Marsman AW, van Rens BJE, de Leeuw DM. *Nat Mater*, 2004, 3: 106–110
3   Subramanian V, Frechet JMJ, Chang PC, Huang DC, Lee JB, Molesa SE, Murphy AR, Redinger DR, Volkman SK. *Proc IEEE*, 2005, 93: 1330–1338
4   Baude PF, Ender DA, Haase MA, Kelley TW, Muyres DV, Theiss SD. *Appl Phys Lett*, 2003, 82: 3964–3966
5   Klauk H, Zschieschang U, Pflaum J, Halik M. *Nature*, 2007, 445: 745–748
6   Sirringhaus H, Kawase T, Friend RH, Shimoda T, Inbasekaran M, Wu W, Woo EP. *Science*, 2000, 290: 2123–2126
7   Crone B, Dodabalapur A, Lin YY, Filas RW, Bao Z, LaDuca A, Sarpeshkar R, Katz HE, Li W. *Nature*, 2000, 403: 521–523
8   Someya T, Dodabalapur A, Huang J, See KC, Katz HE. *Adv Mater*, 2010, 22: 3799–3811
9   Lipomi DJ, Vosgueritchian M, Tee BCK, Hellstrom SL, Lee JA, Fox CH, Bao Z. *Nat Nanotech*, 2011, 6: 788–792
10   Mannsfeld SCB, Tee BCK, Stoltenberg RM, Chen CVHH, Barman S, Muir BVO, Sokolov AN, Reese C, Bao Z. *Nat Mater*, 2010, 9: 859–864
11   Kuribara K, Wang H, Uchiyama N, Fukuda K, Yokota T, Zschieschang U, Jaye C, Fischer D, Klauk H, Yamamoto T, Takimiya K, Ikeda M, Kuwabara H, Sekitani T, Loo YL, Someya T. *Nat Commun*, 2012, 3: 723
12   Roberts ME, Mannsfeld SCB, Queralto N, Reese C, Locklin J, Knoll W, Bao Z. *Proc Natl Acad Scis*, 2008, 105: 12134–12139
13   Berggren M, Richter-Dahlfors A. *Adv Mater*, 2007, 19: 3201–3213
14   Meijer EJ, de Leeuw DM, Setayesh S, van Veenendaal E, Huisman BH, Blom PWM, Hummelen JC, Scherf U, Klapwijk TM. *Nat Mater*, 2003, 2: 678–682
15   Sirringhaus H. *Adv Mater*, 2005, 17: 2411–2425
16   Allard S, Forster M, Souharce B, Thiem H, Scherf U. *Angew Chem Int Ed*, 2008, 47: 4070–4098
17   Anthony JE. *Angew Chem Int Ed*, 2008, 47: 452–483
18   Kwak D, Lim JA, Kang B, Lee WH, Cho K. *Adv Funct Mater*, 2013, 23: 5224–5231
19   Sokolov AN, Cao Y, Johnson OB, Bao Z. *Adv Funct Mater*, 2012, 22: 175–183
20   Fu YT, Yi YP, Coropceanu V, Risko C, Aziz SG, Brédas JL. *Sci China Chem*, 2014, 57: 1330–1339
21   He Z, Chen J, Sun Z, Szulczewski G, Li D. *Organic Electrons*, 2012, 13: 1819–1826
22   Chen J, Tee CK, Shtein M, Anthony J, Martin DC. *J Appl Phys*, 2008, 103: 114513–114513
23   Kushida T, Nagase T, Naito H. *Organic Electrons*, 2011, 12: 2140–2143
24   Chae GJ, Jeong SH, Baek JH, Walker B, Song CK, Seo JH. *J Mater*

Chem C, 2013, 1: 4216–4221

25 Hwang DK, Fuentes-Hernandez C, Berrigan JD, Fang Y, Kim J, Potscavage WJ, Cheun H, Sandhage KH, Kippelen B. *J Mater Chem*, 2012, 22: 5531–5537

26 Lee WY, Oh JH, Suraru SL, Chen WC, Würthner F, Bao Z. *Adv Funct Mater*, 2011, 21: 4173–4181

27 Giri G, Verploegen E, Mannsfeld SCB, Atahan-Evrenk S, Kim DH, Lee SY, Becerril HA, Aspuru-Guzik A, Toney MF, Bao Z. *Nature*, 2011, 480: 504–508

28 Diao Y, Tee BCK, Giri G, Xu J, Kim DH, Becerril HA, Stoltenberg RM, Lee TH, Xue G, Mannsfeld SCB, Bao Z. *Nat Mater*, 2013, 12: 665–671

29 Diao Y, Zhou Y, Kurosawa T, Shaw L, Wang C, Park S, Guo Y, Reinspach JA, Gu K, Gu X, Tee BCK, Pang C, Yan H, Zhao D, Toney MF, Mannsfeld SCB, Bao Z. *Nat Commun*, 2015, 6: 7955

30 Becerril HA, Roberts ME, Liu Z, Locklin J, Bao Z. *Adv Mater*, 2008, 20: 2588–2594

31 Yuan Y, Giri G, Ayzner AL, Zoombelt AP, Mannsfeld SCB, Chen J, Nordlund D, Toney MF, Huang J, Bao Z. *Nat Commun*, 2014, 5: 3005

32 Takimiya K, Osaka I, Mori T, Nakano M. *Acc Chem Res*, 2014, 47: 1493–1502

33 Zheng X, Geng H, Yi Y, Li Q, Jiang Y, Wang D, Shuai Z. *Adv Funct Mater*, 2014, 24: 5531–5540

34 Takimiya K, Kunugi Y, Konda Y, Ebata H, Toyoshima Y, Otsubo T. *J Am Chem Soc*, 2006, 128: 3044–3050

35 Shi W, Chen J, Xi J, Wang D, Shuai Z. *Chem Mater*, 2014, 26: 2669–2677

36 Wang J, Wolf RM, Caldwell JW, Kollman PA, Case DA. *J Comput Chem*, 2004, 25: 1157–1174

37 Wang D, Tang L, Long M, Shuai Z. *J Phys Chem C*, 2011, 115: 5940–5946

38 Gaussian 09, Revision E.01, Frisch, M. J; Trucks, G. W; Schlegel, H. B; Scuseria, G. E; Robb, M. A; Cheeseman, J. R; Scalmani, G; Barone, V; Mennucci, B; Petersson, G. A; Nakatsuji, H; Caricato, M;

Li, X; Hratchian, H. P; Izmaylov, A. F; Bloino, J; Zheng, G; Sonnenberg, J. L; Hada, M; Ehara, M; Toyota, K; Fukuda, R; Hasegawa, J; Ishida, M; Nakajima, T; Honda, Y; Kitao, O; Nakai, H; Vreven, T; Montgomery, J. A., Jr; Peralta, J. E; Ogliaro, F; Bearpark, M; Heyd, J. J; Brothers, E; Kudin, K. N; Staroverov, V. N; Kobayashi, R; Normand, J; Raghavachari, K; Rendell, A; Burant, J. C; Iyengar, S. S; Tomasi, J; Cossi, M; Rega, N; Millam, J. M; Klene, M; Knox, J. E; Cross, J. B; Bakken, V; Adamo, C; Jaramillo, J; Gomperts, R; Stratmann, R. E; Yazyev, O; Austin, A. J; Cammi, R; Pomelli, C; Ochterski, J. W; Martin, R. L; Morokuma, K; Zakrzewski, V. G; Voth, G. A; Salvador, P; Dannenberg, J. J; Dapprich, S; Daniels, A. D; Farkas, Ö; Foresman, J. B; Ortiz, J. V; Cioslowski, J; Fox, D. J. Gaussian, Inc., Wallingford CT, 2009

39 Bayly CI, Cieplak P, Cornell W, Kollman PA. *J Phys Chem*, 1993, 97: 10269–10280

40 Cornell WD, Cieplak P, Bayly CI, Gould IR, Merz KM, Ferguson DM, Spellmeyer DC, Fox T, Caldwell JW, Kollman PA. *J Am Chem Soc*, 1995, 117: 5179–5197

41 Plimpton S. *J Comp Phys*, 1995, 117: 1–19

42 Nosé S. *J Chem Phys*, 1984, 81: 511–519

43 Hoover WG. *Phys Rev A*, 1985, 31: 1695–1697

44 Blöchl PE. *Phys Rev B*, 1994, 50: 17953–17979

45 Grimme S. *J Comput Chem*, 2006, 27: 1787–1799

46 Kresse G, Furthmüller J. *Phys Rev B*, 1996, 54: 11169–11186

47 Perdew JP, Chevary JA, Vosko SH, Jackson KA, Pederson MR, Singh DJ, Fiolhais C. *Phys Rev B*, 1992, 46: 6671–6687

48 Nan G, Li Z. *Phys Chem Chem Phys*, 2012, 14: 9451–9459

49 Diao Y, Lenn KM, Lee WY, Blood-Forsythe MA, Xu J, Mao Y, Kim Y, Reinspach JA, Park S, Aspuru-Guzik A, Xue G, Clancy P, Bao Z, Mannsfeld SCB. *J Am Chem Soc*, 2014, 136: 17046–17057

50 Wang LJ, Li QK, Shuai Z. *J Chem Phys*, 2008, 128: 194706–194706

51 Kubo T, Häusermann R, Tsurumi J, Soeda J, Okada Y, Yamashita Y, Akamatsu N, Shishido A, Mitsui C, Okamoto T, Yanagisawa S, Matsui H, Takeya J. *Nat Commun*, 2016, 7: 11156